

Article

Photoelectrocatalytic Reduction of Cr(VI) in Wastewater with a CuBi_2O_4 Thin Film Photocathode

Sai An ^{1,2,†}, Ying Wang ^{3,†}, Huajian Qiao ², Hao Xiu ², Deyu Liu ^{2,*}  and Yongbo Kuang ^{2,4,*} 

¹ School of Materials Science and Chemical Engineering, Ningbo University, Ningbo 315211, China; ansai@nimte.ac.cn

² Key Laboratory of Advanced Fuel Cells and Electrolyzers Technology of Zhejiang Province, Ningbo Institute of Materials, Technology and Engineering, Chinese Academy of Sciences, 1219 Zhongguan West Road, Ningbo 315201, China

³ Institute of Materials, Ningbo University of Technology, Ningbo 315211, China; wangying@nbut.edu.cn

⁴ Center of Materials Science and Optoelectronics Engineering, University of Chinese Academy of Sciences, Beijing 100049, China

* Correspondence: liudeyu@nimte.ac.cn (D.L.); kuangyongbo@nimte.ac.cn (Y.K.)

† These authors contributed equally to this work.

Abstract: Photoelectrocatalytic approaches show promise for contaminate removal in wastewater through redox reactions. However, the direct treatment of very low concentration heavy metals is a challenging task. Copper bismuth oxide is considered as a potential photocathode material due to its appropriate bandgap width and excellent light absorption properties. In this work, we utilize copper bismuth oxide photoelectrodes with micrometer-scale pores to achieve the efficient and complete reduction of micromolar-level hexavalent chromium(VI) in wastewater. In a continuous 180 min experiment, the reduction rate of 5 μM hexavalent chromium reached 97%, which is an order lower than the drinking standard. Such a process was facilitated by the unique hierarchical microstructure of the oxide thin film and the porous morphology. On the other hand, the structural evolution during the operation was analyzed. A surface passivation was observed, suggesting the possible long-term practical application of this material. This study serves as an important reference for the application of photoelectrocatalysis in addressing Cr(VI) pollution in wastewater, with implications for improving water quality and environmental protection.

Keywords: photoelectrocatalytic; copper bismuth oxide; hexavalent chromium; low concentration



Citation: An, S.; Wang, Y.; Qiao, H.; Xiu, H.; Liu, D.; Kuang, Y.

Photoelectrocatalytic Reduction of Cr(VI) in Wastewater with a CuBi_2O_4 Thin Film Photocathode. *Catalysts* **2024**, *14*, 289. <https://doi.org/10.3390/catal14050289>

Academic Editors: Vincenzo Vaiano and Olga Sacco

Received: 22 March 2024

Revised: 17 April 2024

Accepted: 23 April 2024

Published: 25 April 2024



Copyright: © 2024 by the authors. Licensee MDPI, Basel, Switzerland. This article is an open access article distributed under the terms and conditions of the Creative Commons Attribution (CC BY) license (<https://creativecommons.org/licenses/by/4.0/>).

1. Introduction

In the contemporary world, the issue of water pollution is increasingly drawing the attention of society, especially heavy metal contaminations including hexavalent chromium (Cr(VI)) [1]. As a crucial component widely employed in various industrial processes, Cr(VI) exhibits high toxicity and carcinogenicity, posing significant threats to both the environment and human health [2]. Experiments have shown that the ingestion of water containing hexavalent chromium leads to its absorption by cells in various tissues and organs, resulting in cancer [3]. The World Health Organization has set the maximum permissible level of Cr(VI) in drinking water as 50 $\mu\text{g}/\text{L}$. The establishment of stringent standards for hexavalent chromium is precisely because even at low concentrations it exhibits a certain degree of toxicity [4]. The absorption and gradual accumulation of low concentrations of Cr(VI) from industrial wastewater discharge by organisms lead to bioaccumulation, posing potential implications for human health in the long term. In view of this, addressing low concentrations of Cr(VI) in wastewater is imperative.

Presently, a wealth of literature exists on hexavalent chromium, encompassing diverse treatment modalities such as ion exchange, membrane separation, adsorption, electrochemical precipitation, and photocatalysis [5–8]. However, these methods are generally

characterized by high energy consumption, high costs, low efficiency, and incomplete removal, which hinder their widespread application. These methodologies have shown significant efficacy and potential in addressing the high concentrations of Cr(VI) solutions. Nevertheless, it is pertinent to note that investigations targeting the removal of low concentrations of Cr(VI) remain relatively limited. In recent years, photoelectrochemistry (PEC) approaches have gained a considerable amount of attention as an emerging technology for their high selectivity and efficiency during operation [9,10]. The existing literature reports the use of TiO₂ thin films for photoelectrochemical reduction of hexavalent chromium (Cr(VI)) [11–13]. Wang et al. employed a sensitization method with Ag₂S and Bi₂S₃ to prepare TiO₂ nanoelectrodes, achieving a removal efficiency of 92.4% of Cr(VI) within 3 h [14]. However, TiO₂ has a wide bandgap width, allowing only 5% of the solar energy to be absorbed, rendering it inefficient in utilizing visible light and severely limiting its application prospects. Other semiconductors such as WO₃/BiVO₄ [15], although also applied in the PEC reduction of Cr(VI) systems, exhibit similar drawbacks to those mentioned above. Moreover, the preparation of composite materials requires complex synthesis processes and involves higher production costs. Hence, the pursuit of semiconductor photoelectrodes tailored for the cost-effective and efficient photoelectrocatalytic reduction of Cr(VI) has emerged as a new research hotspot.

Copper bismuth oxide (CuBi₂O₄) has garnered extensive attention and application in the field of photoelectrocatalysis due to its structural characteristics [16–19]. For instance, CuBi₂O₄ is employed as a photocatalyst for photoelectrochemical water splitting to produce hydrogen [20,21] and for the photoelectrochemical reduction of CO₂ to generate methane and other fuels [22,23]. Additionally, CuBi₂O₄ serves as a key component in photoelectrochemical sensors for detecting various chemical substances in the environment [24]. In recent years, CuBi₂O₄ has shown significant potential as a photocathode material for addressing the reduction of Cr(VI). On the one hand, CuBi₂O₄ possesses a bandgap width of 1.5–1.8 eV [25], exhibiting excellent light absorption in the visible range and effectively utilizing visible light. On the other hand, the conduction band minimum (CBM) of CuBi₂O₄ is positioned more negatively than the thermodynamic potential for Cr(VI) reduction, providing the theoretical basis for the application of CuBi₂O₄ in the PEC reduction of Cr(VI). Kumar et al. utilized CuBi₂O₄/Bi/CuFe₂O₄ heterojunctions for simultaneous photocatalytic degradation of both ICP and Cr(VI), achieving an 88.7% reduction of Cr(VI) under sunlight [26]. Zhang et al. also employed CBO/CLDHs composite materials for the adsorption and photocatalytic reduction of Cr(VI) and tetracycline, achieving a 95% reduction rate for Cr(VI) at an initial concentration of 40 mg/L [27]. These studies provide feasible research directions for utilizing copper bismuth oxide in the reduction of Cr(VI).

Although CuBi₂O₄ has demonstrated potential in the reduction of Cr(VI), current research heavily relies mainly on heterogeneous structures, resulting in high costs and complex fabrication processes, thereby limiting practical applications. To address this issue, our study employed a singular copper bismuth oxide material for the reduction of low-concentration Cr(VI). We successfully prepared copper bismuth oxide films with micrometer-scale porous structures using a spray pyrolysis method, which helps to improve the reduction of Cr(VI). Furthermore, in order to overcome slow diffusion in low-concentration solutions, we introduced a flow cell system, enabling more efficient reactions. This study not only tackles the cost and fabrication challenges associated with heterogeneous structures of CuBi₂O₄ but also provides new insights and methodologies for its application in the reduction of low-concentration Cr(VI).

2. Results and Discussion

2.1. Characterization of CuBi₂O₄ Thin Film Photoelectrode

Due to the exceedingly low concentration of Cr(VI) in the reaction substrate, mass transfer has become the primary limiting factor affecting the efficacy of the photoelectrode in water treatment. The SEM images display the microstructures of two CuBi₂O₄ thin film photoelectrodes with distinct structural characteristics. The low magnification images in

the insets provide a clearer observation of the pore sizes. The CuBi_2O_4 thin film depicted in Figure 1a exhibits a porous structure at the micrometer scale, whereas the film in Figure 1b features a structure with a small number of nanoscale pores. In order to identify the phases of the two samples, X-ray diffraction patterns were measured. As shown in Figure 1c, peaks at 20.9° , 28.1° , 29.7° , 30.9° , 33.4° , 46.8° , 53.2° , and 55.8° can be indexed as CuBi_2O_4 , consistent with the JCPDF standard card no. 48-1886, indicating the successful preparation of the CuBi_2O_4 thin film. No other crystal phases were observed in the XRD pattern, demonstrating the high purity and good crystallinity of the prepared sample.

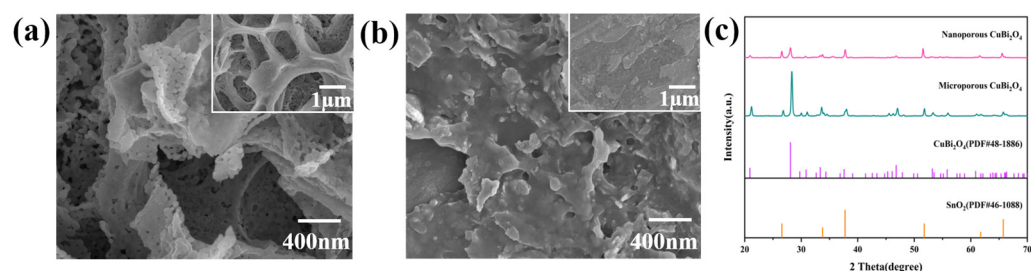


Figure 1. (a) SEM images of microporous CuBi_2O_4 ; (b) SEM images of microporous CuBi_2O_4 ; (c) the XRD spectra of the two CuBi_2O_4 thin films.

The design of CuBi_2O_4 thin film photoelectrodes with a porous structure at the micrometer scale is motivated by the following consideration: During the photocatalytic reaction in low-concentration solutions, a more open structure is required to allow a large volume of solution to flow through the electrode, facilitating a thorough reaction. Dong et al. found that the PEC rate constant of porous thin films was approximately three times higher than that of compact samples when utilizing BiVO_4 to degrade MB fuel solutions [28]. Wen et al. also observed that the photocurrent of porous photocathodes was three times higher than that of dense electrodes when studying $\text{Cu}_2\text{ZnSnS}_4$ [29]. Furthermore, the literature suggests that photocatalysts with a porous structure, due to their large surface area and abundant porosity, provide active sites for the effective transport of catalytic reactions and intermediates, thereby enhancing catalytic performance [30–32]. Based on the research on the relationship between film porosity structure and its photoelectric performance described above, we speculate that copper bismuth oxide electrodes with larger pore structures may be more favorable for the reduction of hexavalent chromium at low concentrations.

2.2. Photoelectrochemical Properties

Typical PEC tests of the CuBi_2O_4 thin film are shown in Figure 2. The linear sweep voltammetry (LSV) curve of the microporous CuBi_2O_4 was tested in $5 \mu\text{M}$ $\text{K}_2\text{Cr}_2\text{O}_7$ (pH 6.5 citrate buffer) as Figure 2a. Under a 455 nm LED ($39 \text{ mW}/\text{cm}^2$) light source, the photocurrent density is $0.05 \text{ mA}/\text{cm}^2$ @ 0.6 V vs. RHE. Figure 2b,c, respectively, show the LSV curves of the microporous CuBi_2O_4 thin film electrode in $\text{K}_2\text{Cr}_2\text{O}_7$ solutions of different concentrations under light and dark conditions. It is evident from the graphs that the photocurrent increases with the concentration of Cr(VI), indicating that the PEC activity of CuBi_2O_4 thin film electrodes in $\text{K}_2\text{Cr}_2\text{O}_7$ solutions is influenced by the chromium concentration under illumination. However, despite its rising photocurrent trend, it does not exhibit a linear relationship. The increase in chromium concentration may induce changes in the reaction kinetics, such as variations in electron transfer rates or adsorption kinetics of reaction products, potentially leading to a nonlinear increase in current response.

Meanwhile, we conducted LSV tests on the reaction of the nanoporous CuBi_2O_4 photoelectrodes in $\text{K}_2\text{Cr}_2\text{O}_7$ solutions of various concentrations, as shown in Figure S4. Through the comparison of results, we found that at the same chromium concentration, the photocurrent of the microporous CuBi_2O_4 is always greater than that of the nanoporous CuBi_2O_4 . This phenomenon may be attributed to the larger pores and surface area of the microporous CuBi_2O_4 . During the photoelectrocatalytic reduction process of Cr(VI), this

larger pore structure provides increased reaction interfaces, which afford more opportunities for interactions between photogenerated electrons and hexavalent chromium ions. Furthermore, the larger pore structure demonstrates higher diffusion rates and conductivity, facilitating accelerated transport of photogenerated electrons and relevant species.

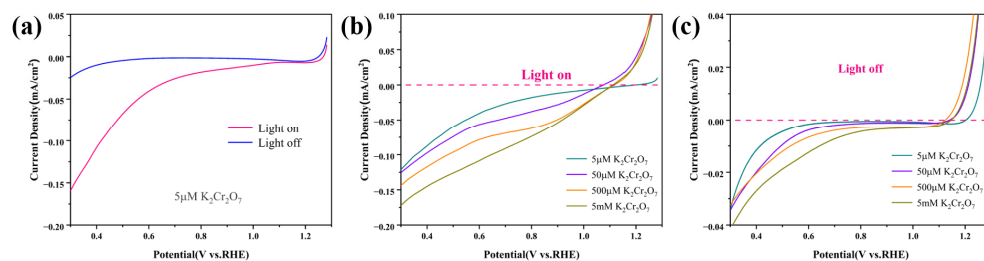


Figure 2. PEC tests of microporous CuBi_2O_4 thin film photoelectrodes; (a) LSV tests of CuBi_2O_4 film photoelectrodes in $5 \mu\text{M}$ $\text{K}_2\text{Cr}_2\text{O}_7$ solution; (b,c) LSV tests of CuBi_2O_4 thin film photoelectrodes in $5 \mu\text{M}$ – 5mM $\text{K}_2\text{Cr}_2\text{O}_7$ solution under light and dark conditions.

To investigate the internal charge transfer behavior of the CuBi_2O_4 photocathode in the Cr(VI) solution, impedance spectroscopy measurements were conducted on two types of CuBi_2O_4 thin film photoelectrodes at 0.6 V vs. RHE . The impedance spectrum shown in Figure 3a indicates that the microporous structure of the CuBi_2O_4 thin film electrode exhibits a smaller arc radius compared to the nanoporous CuBi_2O_4 , demonstrating the lower charge transfer resistance of the electrode. This implies enhanced efficacy in charge transfer and separation within the electrode structure. In the PEC reduction of low-concentration Cr(VI) , the effective separation and transfer of photo-generated charge carriers are crucial. The electron-hole pairs generated upon light absorption need to rapidly separate within the catalyst, and transfer to the electrode surface to participate in the PEC reduction reaction. Photoelectrodes like CuBi_2O_4 with microporous structures can offer increased surface area and active sites, facilitating higher efficiency in the separation of photo-generated electron-hole pairs and promoting the transfer of photo-generated charges carriers to the catalytic surface, thereby enhancing the efficiency of the PEC reduction of Cr(VI) .

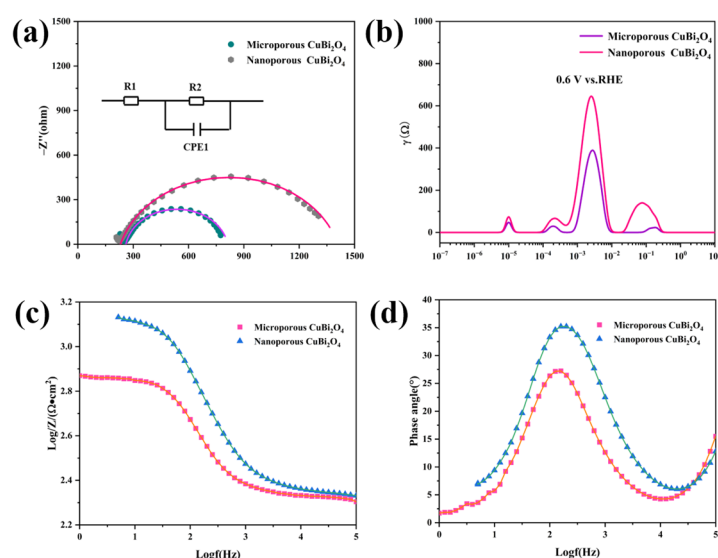


Figure 3. (a) Impedance spectra were measured at 0.6 V vs. RHE for microporous and nanoporous CuBi_2O_4 photocathodes. The solid lines represent the fitting data using the corresponding equivalent circuit; (b) the corresponding DRT plots; (c,d) the corresponding Bode plot.

Figure 3b illustrates the corresponding distribution of the distributed relaxation time (DRT) for both electrodes. It is observed that the DRT plot of the microporous CuBi_2O_4 rela-

tive to the nanoporous CuBi_2O_4 exhibits a lower peak in the midfrequency region, indicating lower interfacial resistance and a slower charge carrier recombination rate. In Figure 3c,d, the Bode plots of two photoelectrodes are displayed. It is observed that both exhibit peaks at low frequencies. Furthermore, the Bode plot of the microporous CuBi_2O_4 thin film electrode demonstrates minimal phase variation within the system. These observations indicate enhanced stability of the catalytic reaction within the microporous CuBi_2O_4 thin film photoelectrode system. Collectively, these characteristics promote rapid transfer of charge carriers at the electrode–electrolyte interface and effective utilization of photo-generated charges, thereby enhancing the performance of the photoelectrocatalytic reaction.

2.3. Photoelectrocatalytic Reduction of Cr(VI)

Drawing from the analysis above, we have decided to employ the microporous CuBi_2O_4 photoelectrode as the catalyst for the PEC reduction of Cr(VI). Prior to the reduction of Cr(VI), we conducted an exploration of the issue concerning the detection of Cr(VI). For the identification of reduced Cr(VI), we employed the DPD colorimetric method [33]. We investigated the colorimetric reaction between Cr(VI) and DPD within the range of 0–10 μM . Subsequently, calibration curves for Cr(VI) were constructed based on the absorption spectra obtained at 510 nm and 551 nm after a 30 min reaction and accompanied with the R^2 values greater than 99.9%, as illustrated in Figure S5.

We employed the 5 μM $\text{K}_2\text{Cr}_2\text{O}_7$ solution as the initial concentration for the reaction and utilized the CuBi_2O_4 thin film as the photocathode to perform the PEC reduction reaction in a flow cell. The detailed specifications of the flow cell are outlined in Figure S3. Subsequently, Cr(VI) samples with different reduction times were mixed with 15 mM DPD for a 30 min color reaction, as shown in Figure 4a. The color changes in the solution indicate that Cr(VI) undergoes further reduction with prolonged time. The absorption spectra of the $\text{DPD}^{\bullet+}$ radicals produced from the reaction between Cr(VI) solution and DPD at different reduction times were recorded in the range of 400–600 nm, as illustrated in Figure 4b. The characteristic absorbance at 551 nm was used to track the concentration of Cr(VI). The graph clearly demonstrates that the concentration of Cr(VI) decreases with time, consistent with visual observations. Figure 4c depicts the trend of the Cr(VI) concentration over time. It can be observed that the decrease in PEC of Cr(VI) exhibits an almost linear trend in the initial 40 min, but significantly decreases in the longer reduction times. This phenomenon may be attributed to changes in reaction kinetics as Cr(VI) concentration decreases, leading to a slower reaction rate. According to the reaction kinetics model, the reaction initially approximates zero-order kinetics, but as reactants are consumed, mass transfer at very low concentrations becomes the limiting factor. At this point, the reaction rate may begin to be influenced by reactant concentration, gradually transitioning to first-order kinetics. This indicates that the transfer rate of Cr(VI) in the reaction is slower than the catalytic reaction rate, and the diffusion of Cr(VI) in the reaction system remains limited.

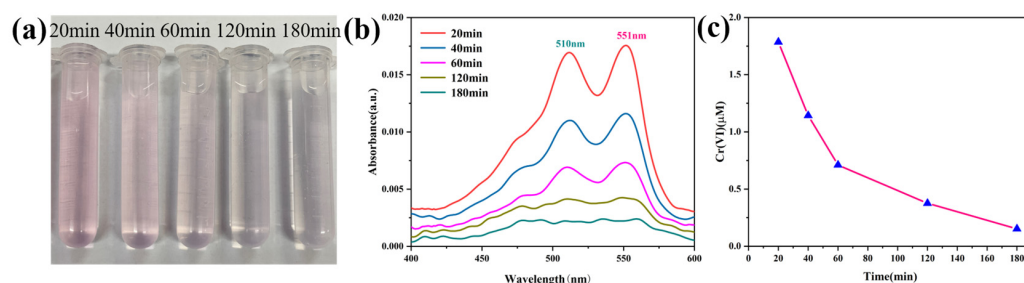


Figure 4. (a) Color change and (b) absorbance spectrum of $\text{DPD}^{\bullet+}$ generated by DPD with $\text{K}_2\text{Cr}_2\text{O}_7$ after PEC reduction for different durations, followed by reaction. Conditions: pH = 6.5 (0.1 M CA buffer), [DPD] = 15 mM, and reaction time at 30 min. (c) Trend plot of Cr(VI) concentration after different reduction times.

The reduction percentages after subjecting the same 5 μM Cr(VI) to reduction for varying durations are presented in Table 1. It is evident that after 20 min of photoelectrocatalytic reduction of 5 μM Cr(VI), its concentration decreased to 1.79 μM , corresponding to a reduction rate of 64%. Following the 40 min PEC reduction, the concentration decreased to 1.14 μM , which meets international drinking water standards. Subsequently, we extended the reduction time, and after 60 min, 120 min, and 180 min of reduction of the same Cr(VI) solution, the reduction percentages reached 86%, 92%, and 97%, respectively.

Table 1. Cr(VI) concentration and reduction rate after different reduction times.

Time (min)	Cr(VI) (μM)	Reduction Percentage
20	1.79	64%
40	1.14	77%
60	0.71	86%
120	0.38	92%
180	0.15	97%

2.4. Evaluation of Microporous CuBi_2O_4 Characteristics

This study investigates the application of the microporous CuBi_2O_4 photoelectrode in the PEC reduction of hexavalent chromium at low concentrations. We performed a 3 h chronoamperometry (CA) stability test on microporous CuBi_2O_4 in the 5 μM $\text{K}_2\text{Cr}_2\text{O}_7$ solution at 0.6 V vs. RHE.

As illustrated in Figure 5a, the photocurrent curve exhibits a significant decay within the initial 20 min, which can be attributed to the interfacial chemical evolutions of the photoelectrode during the initial stages of the reaction, namely the formation of oxides or other substances such as metal particles of copper/bismuth. In the SEM images presented in Figure S6, we observed the appearance of subtle fine particles on the sample surface following the PEC reduction reaction, which confirms the formation of additional substances on the electrode surface.

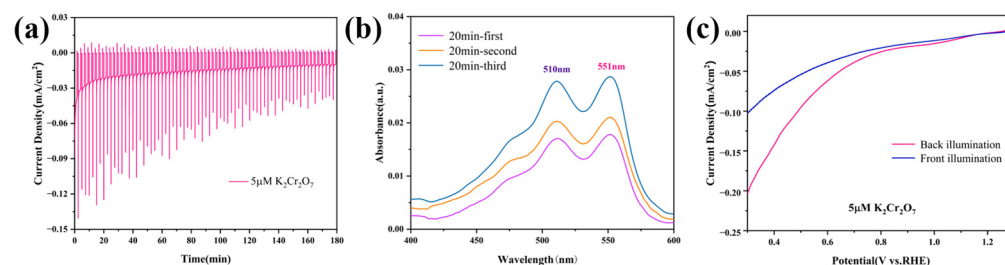


Figure 5. (a) CA testing of microporous CuBi_2O_4 ; (b) absorbance of three samples of 5 μM Cr(VI) after successive PEC reduction with the same CuBi_2O_4 thin film; (c) the LSV test for microporous CuBi_2O_4 under front and back illumination.

In order to investigate the reusability of the CuBi_2O_4 photoelectrode in the photoelectrocatalytic reduction of Cr(VI), we sequentially subjected three identical 5 μM Cr(VI) solutions to consecutive 20 min photoelectrocatalytic reduction processes using the same CuBi_2O_4 thin film as the catalyst. The absorbance of the Cr(VI) solutions reacting with the DPD colorimetric agent was measured, as shown in Figure 5b. We observed that with repeated use of CuBi_2O_4 , the Cr(VI) solutions continued to undergo reduction, but their reduction efficiency gradually decreased. This further confirms the presence of certain corrosion phenomena in the CuBi_2O_4 thin film within this reaction system.

Figure 5c presents the comparison of LSV for the CuBi_2O_4 thin film photoelectrode under back illumination and front illumination in the $\text{K}_2\text{Cr}_2\text{O}_7$ solution. The photocurrent under back illumination is significantly higher than that under front illumination. This is attributed to the fact that under back illumination conditions, photogenerated electrons are more likely to migrate directly to the catalytic surface and participate in catalytic reactions,

thereby enhancing the utilization efficiency of the photogenerated electrons. This direct migration path of photogenerated electrons helps to reduce losses during the electron transfer process.

Through X-ray photoelectron spectroscopy (XPS) analysis, we conducted a detailed investigation into the surface elemental composition and chemical states of the microporous CuBi_2O_4 photoelectrode. In Figure 6a, the XPS spectrum of Cu 2p exhibits four peaks: two prominent peaks located at 933.4 and 953.4 eV, corresponding to Cu 2p_{3/2} and Cu 2p_{1/2}, respectively, and two satellite peaks near 943.2 and 962.0 eV. These prominent peaks confirm the chemical state of Cu^{2+} , while the two satellite peaks in the spectrum further confirm the predominant Cu valence state as +2 [34,35]. Figure 6b displays the XPS spectrum of Bi 4f, with a peak observed at 158.7 eV corresponding to Bi 4f_{7/2} and a binding energy peak at 163.9 eV corresponding to Bi 4f_{5/2}. This clearly indicates the presence of Bi in the photoelectrode in the +3 chemical state [36]. As shown in Figure 6c, the O 1s spectrum can be decomposed into a Bi³⁺-lattice oxygen binding at 531.4 eV and a Cu²⁺-lattice oxygen binding at 529.4 eV [37]. These XPS results further validate the successful preparation of the CuBi_2O_4 sample, consistent with the X-ray diffraction (XRD) test results.

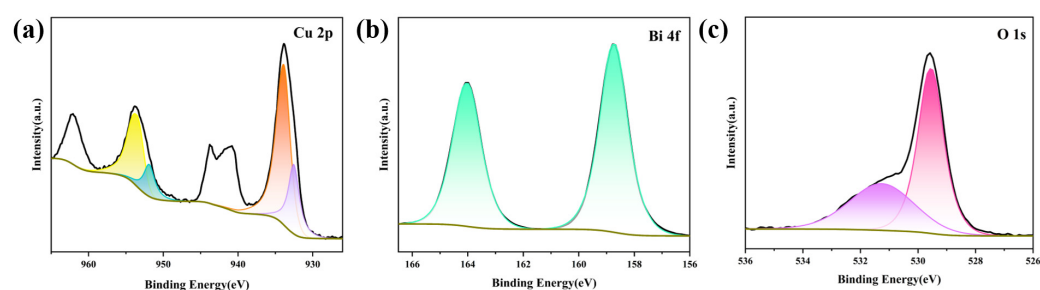


Figure 6. XPS spectra of microporous CuBi_2O_4 thin film photoelectrodes (a) Cu 2p; (b) Bi 4f; (c) O 1s.

XPS analysis (Figure S7) of the CuBi_2O_4 photoelectrode before and after the reaction revealed peak shifts of Cu 2p, Bi 4f, and O1s within only 0.5 eV, indicating minor variations possibly due to subtle ambient contaminations. Additionally, the pie chart in Figure S8 obtained through full-spectrum analysis, showed a decrease in both Cu and Bi contents on the CuBi_2O_4 photoelectrode surface after the reaction. Trace amounts of Cr were detected on the CuBi_2O_4 surface post-reaction, suggesting potential corrosion of the CuBi_2O_4 photoelectrode during the reaction. On the other hand, as the photocurrent decays, the Faradaic efficiency may decrease because photogenerated electrons are utilized to reduce Cr(VI) ions, forming reduced chromium species on the electrode surface. As the reaction progresses, the concentration of Cr(VI) ions decreases, reducing the available species for photogenerated electron reduction. Consequently, as the reaction proceeds, the utilization efficiency of photogenerated electrons decreases, leading to a decline in photocurrent. This phenomenon indicates the formation of a passivation layer on the electrode surface as the reaction proceeds, limiting further photoelectrocatalytic reactions and resulting in the decay of photocurrent.

Based on the above experiments and results, the mechanism of CuBi_2O_4 thin film as a photocathode for the photoelectrocatalytic reduction of Cr(VI) can be proposed, as illustrated in Figure 7. The specific process is as follows:



When light with energy greater than the bandgap is irradiated onto the surface of the CuBi_2O_4 catalyst, electrons within it are excited, transitioning from the valence band to the conduction band, forming electron-hole pairs. Subsequently, these photogenerated

electrons and holes quickly migrate to the semiconductor surface after spatial charge separation. During this process, photogenerated electrons migrate to the surface of the photocathode and come into contact with Cr(VI) ions in the solution. Since the conduction band minimum (CBM) of CuBi_2O_4 is situated at a more negative thermodynamic potential compared to the reduction potential of Cr(VI), it can reduce it to non-toxic Cr(III) ions. Additionally, the valence band maximum (VBM) of CuBi_2O_4 is situated at 0.8 V vs. NHE, preventing the re-oxidation of already reduced Cr(III) ions in the reaction system, thereby achieving the removal of hexavalent chromium. Meanwhile, the holes participate in oxidation reactions by transferring through the external circuit to the electrode surface, leading to the production of oxygen or other oxidation products.

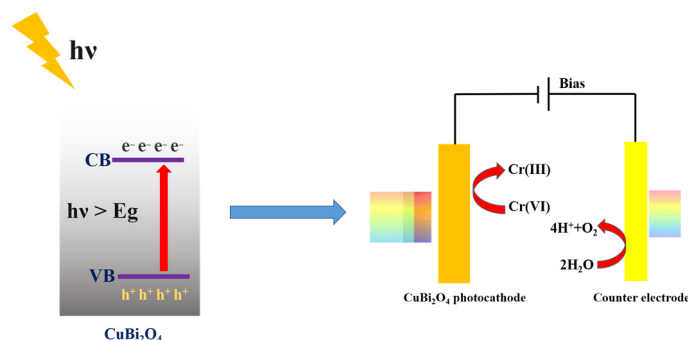


Figure 7. Schematic illustration for the PEC reduction of Cr(VI) over CuBi_2O_4 photoelectrodes under visible light irradiation.

3. Materials and Methods

3.1. Preparation of CuBi_2O_4 Composite Photoelectrode

The potassium dichromate, ethanol, and polyvinyl alcohol used in the experiment were purchased from China National Medicines Corporation Ltd. (Beijing, China), while other chemicals were procured from Aladdin (Shanghai, China). The preparation method for the precursor solution of CuBi_2O_4 is as follows: 315 mg of $\text{C}_6\text{H}_8\text{O}_7 \cdot \text{H}_2\text{O}$ and 485 mg of $\text{Bi}(\text{NO}_3)_3 \cdot \text{H}_2\text{O}$ were mixed in 50 mL of deionized water, followed by ultrasonic homogenization and filtration to obtain bismuth citrate, which was then dried for later use. Subsequently, 525 mg of $\text{C}_6\text{H}_8\text{O}_7 \cdot \text{H}_2\text{O}$ was dissolved in 1 mL of deionized water and mixed with 600 μL of $\text{NH}_3 \cdot \text{H}_2\text{O}$. The dried bismuth citrate was added to the solution and sonicated until completely clarified. Then, 42 mL of deionized water was added and mixed thoroughly, followed by the addition of 100 mg of $\text{Cu}(\text{CO}_2\text{CH}_3)_2 \cdot \text{H}_2\text{O}$, stirred until completely dissolved. Finally, polyvinyl alcohol (5 mL, 0.1%) and Triton X-100 (100 μL , 0.2%) were added. Additionally, a precursor solution for dense CuBi_2O_4 thin films was prepared using a molar ratio of 1:2 for $\text{Cu}(\text{NO}_3)_2$ and $\text{Bi}(\text{NO}_3)_3$ in a 9:1 ethanol/acetic acid solution. Porous thin films were prepared on fluorine-doped tin oxide glass substrates using the spray pyrolysis technique. Ultrasonic nozzles with droplet diameter distribution ranging from 20 to 100 μm (operated at 120 kHz) were employed for atomization. Uniform deposition coverage was achieved by employing a motorized platform for programmed x-y motion with multicycles. Each movement from one side to the other side of the substrates is defined as “one lap”. The schematic of the spray route is illustrated in Figure S2. Subsequently, the intermediate film was calcined in a muffle furnace at 450 $^\circ\text{C}$ for 2 h at a heating rate of 5 $^\circ\text{C}/\text{min}$ to obtain the final porous oxide films.

3.2. Characterization

Morphologies of the samples were recorded using a Hitachi (Tokyo, Japan) S4800 Scanning Electron microscope (SEM) operated at 10 kV. The X-ray diffraction (XRD) patterns were obtained on a Bruker (Karlsruhe, Germany) AXS-D8 Advance Davinci diffractometer. X-ray photoelectron spectroscopy (XPS) measurements were performed on a Thermo Scientific (Waltham, MA, USA) K-Alpha. UV-visible (UV-Vis) absorption spectra were

recorded on a Perkin-Elmer (Waltham, MA, USA) Lambda 950 UV-Vis NIR Spectrometer. Additionally, this instrument was utilized to assess the chromogenic reaction of Cr(VI) for the construction of a standard working curve.

3.3. Photoelectrochemical Measurements

The reactor utilized for PEC reduction was a flow cell designed in-house, as illustrated in Figure 8. All photoelectrochemical experiments of CuBi_2O_4 were performed in a flow cell with a three-electrode system comprised of the spray deposited electrode as the working electrode, an Ag/AgCl reference electrode, and an Ni mesh counter electrode.

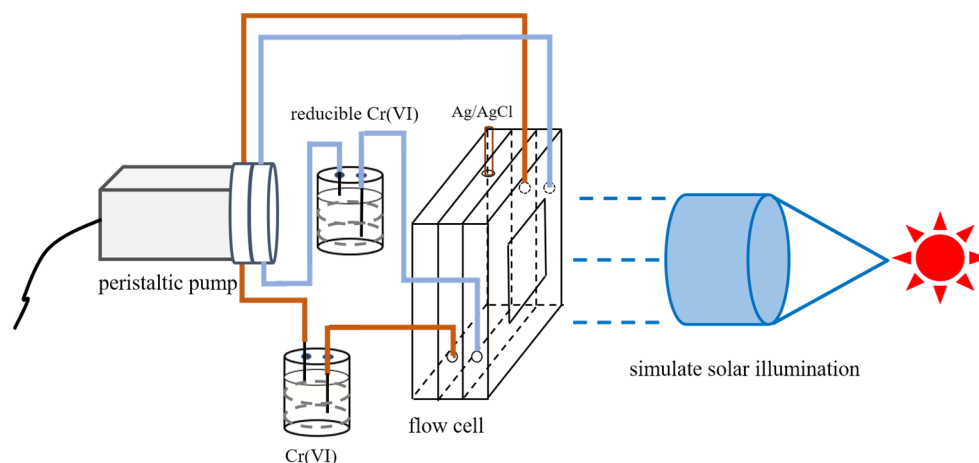


Figure 8. Schematic diagram of self-designed flow cell.

The 0.01 M of citric acid buffer solution was used as the electrolyte for the photoelectrochemical (PEC) measurements. Linear sweep voltammetry (LSV) and chronoamperometry tests (CA) were conducted on a CHI600E electrochemical workstation from Chenhua (Shanghai, China). A 455 nm LED was employed to simulate solar illumination with the intensity of 39 mW/cm^2 . For the photocurrent tests, the as-prepared film photocathodes were measured from 0.7 V to -0.3 V relative to Ag/AgCl using a scan rate of 40 mV/s under light and dark conditions. Subsequently, the electrode potential versus the reversible hydrogen electrode (RHE) is converted from Ag/AgCl electrode on the basis of the formula [38]:

$$E_{\text{RHE}} = E_{\text{Ag/AgCl}} + E_{\text{Ag/AgCl}}^{\theta} + 0.059\text{pH} \quad (4)$$

Electrochemical impedance spectra were measured at 0.6 V vs. RHE, ranging from 10 kHz to 5 Hz with an AC amplitude of 10 mV, by ModuLab (Bucharest, Romania) XM potentiostat.

3.4. Photoelectrocatalytic Tests

To prepare a $100 \mu\text{M}$ Cr(VI) solution as a stock solution, 0.0147 g of $\text{K}_2\text{Cr}_2\text{O}_7$ was dissolved in 500 mL of pH 6.5 citric acid buffer. Subsequently, 5 mL of the stock solution was diluted to 500 mL to create a $5 \mu\text{M}$ Cr(VI) solution as a contaminant stock. A photoelectrochemical reduction of Cr(VI) was performed with the obtained CuBi_2O_4 films ($3 \times 3 \text{ cm}^2$) as the photocathode in a flow cell. A fixed bias voltage of 0.6 V vs. RHE was applied during the reduction process. The illumination and dark conditions were controlled for 100 s and 50 s, respectively.

3.5. Detection of Hexavalent Chromium

A series of Cr(VI) solutions at concentrations of $1 \mu\text{M}$, $3 \mu\text{M}$, $5 \mu\text{M}$, $7 \mu\text{M}$, and $11 \mu\text{M}$ were prepared by diluting the $100 \mu\text{M}$ stock solution. For this purpose, 0.197 g of N,N-diethyl-p-phenylenediamine (DPD) was dissolved in 50 mL of deionized water to obtain a 15 mM DPD stock solution. The 0.25 M pH 4.75 acetic acid buffer was prepared. The

analysis of Cr(VI) using the DPD method was conducted as follows: Prior to measurements, the spectrometer was preheated for 10 min to achieve stable absorbance. In a colorimetric tube, 5.0 mL of acetic acid buffer and 3.0 mL of DPD stock solution were mixed, followed by the addition of 2.0 mL of an unknown concentration of Cr(VI) sample after reduction, and the mixture was allowed to react for 30 min. The colored solutions were then transferred to a quartz cuvette, and the absorbance was measured in the range of 400–600 nm using a UV-Vis spectrometer.

Identical 10 mL 5 μ M $K_2Cr_2O_7$ initial solutions were prepared, with one randomly chosen aliquot serving as a reference without participating in the PEC reduction. The $CuBi_2O_4$ thin film samples prepared under identical conditions were used as photocathodes for the photoelectrocatalytic reduction of various Cr(VI) solutions at different time intervals. The reduced and unreduced Cr(VI) solutions were collected and labelled in glass bottles. After mixing the reduced chromium reagents with DPD for 30 min, UV-visible absorption testing was conducted. Based on the obtained absorbance and the calibration curve, the concentration of reduced hexavalent chromium can be determined. The reduction rate of Cr(VI) was calculated using the following formula:

$$R = (C_0 - C_t) / C_0 \times 100\% \quad (5)$$

C_0 and C_t are the initial and the equilibrium concentrations of Cr(VI) in the solution, respectively.

4. Conclusions

In this study, we successfully synthesized $CuBi_2O_4$ thin film photoelectrodes via the spray pyrolysis method for the efficient reduction of low-concentration Cr(VI). The experimental results demonstrate that the designed $CuBi_2O_4$ photocatalyst achieved a 97% photovoltaic reduction efficiency of Cr(VI) at a concentration of 5 μ M within 180 min. The unique layered structure and porous morphology of the thin film electrode facilitate the efficient PEC reduction process of Cr(VI). Notably, surface passivation phenomena were observed during the repeated use of the electrode, indicating the long-term stability of the $CuBi_2O_4$ photocatalyst suitable for practical wastewater treatment applications. This study provides an effective strategy for the development of highly efficient photocatalysts for the treatment of low-concentration Cr(VI) and offers a feasible solution for pollutant removal in wastewater, potentially making significant contributions to environmental protection.

Supplementary Materials: The following supporting information can be downloaded at: <https://www.mdpi.com/article/10.3390/catal14050289/s1>. Figure S1. Digital photographs of the spray pyrolysis equipment: (a) liquid injection syringe; (b) ultrasonic atomizing nozzle, x-y-z triaxial motion system, and the heating platform; (c) proton flowmeter; (d) air compressor. Figure S2. The schematic of spray route. Figure S3. Flow cell information, structural design and composition. Figure S4. (a,b) LSV testing of nanoporous $CuBi_2O_4$ thin film photoelectrodes in 5 μ M-5 mM $K_2Cr_2O_7$ solution under light and dark conditions. Figure S5. (a) Absorption spectra of Cr(VI) solutions with different concentrations after developing color with DPD for 30 min; (b,c) Calibration curve of DPD method for determining Cr(VI) in the 0–10 μ M range at 510 nm and 551 nm. Figure S6. The SEM images of $CuBi_2O_4$ before and after participating in the photoelectrocatalytic reaction. Figure S7. XPS spectra of $CuBi_2O_4$ thin film photoelectrodes before and after photoelectrocatalytic reduction of Cr(VI) for 3 h; (a) Cu 2p; (b) Bi 4f; (c) O1s; (d) XPS full spectrum. Figure S8. Analysis of element content before and after 3 h of PEC reaction.

Author Contributions: S.A. and Y.W. conceived the idea. S.A., H.Q. and D.L. designed the flow cell. H.X. provided the preparation method. S.A. performed all the experiments. S.A., D.L. and Y.K. analyzed the experiment data. S.A. wrote the manuscript. D.L. and Y.K. helped the writing. S.A., Y.W. and D.L. reviewed and edited the manuscript, and supervised the projects and process. All authors have read and agreed to the published version of the manuscript.

Funding: This research was funded by the National Natural Science Foundation of China (NSFC, Grant No. 22272193), Zhejiang Provincial Natural Science Foundation (LZ21B030001), Ningbo Key Research and Development Project (2023Z147), and Ningbo 3315 Program.

Data Availability Statement: The data that support the findings of this study are available in the Supplementary Materials of this article.

Conflicts of Interest: The authors declare no conflicts of interest.

References

1. Economou-Eliopoulos, M.; Megremi, I. Contamination of the Soil–Groundwater–Crop System: Environmental Risk and Opportunities. *Minerals* **2021**, *11*, 775. [[CrossRef](#)]
2. Babuji, P.; Thirumalaisamy, S.; Duraisamy, K.; Periyasamy, G. Human Health Risks Due to Exposure to Water Pollution: A Review. *Water* **2023**, *15*, 2532. [[CrossRef](#)]
3. Zhitkovich, A. Chromium in Drinking Water: Sources, Metabolism, and Cancer Risks. *Chem. Res. Toxicol.* **2011**, *24*, 1617–1629. [[CrossRef](#)] [[PubMed](#)]
4. Shaw, P.; Mondal, P.; Dey Bhowmik, A.; Bandyopadhyay, A.; Sudarshan, M.; Chakraborty, A.; Chattopadhyay, A. Environmentally Relevant Hexavalent Chromium Disrupts Elemental Homeostasis and Induces Apoptosis in Zebrafish Liver. *Bull. Environ. Contam. Toxicol.* **2022**, *108*, 716–724. [[CrossRef](#)] [[PubMed](#)]
5. Ren, Y.; Han, Y.; Lei, X.; Lu, C.; Liu, J.; Zhang, G.; Zhang, B.; Zhang, Q. A Magnetic Ion Exchange Resin with High Efficiency of Removing Cr (VI). *Colloids Surf. A Physicochem. Eng. Asp.* **2020**, *604*, 125279. [[CrossRef](#)]
6. Peng, C.; Xinwan, Z.; Guangyuan, M.; Tao, F.; Yuanyuan, X.; Zhiwei, W.; Pengfei, S.; Lehua, Z.; Haifeng, L. Construction of Bubbles Enrichment Sites and Gas-Diffusion-Microchannel to Assist Cr(VI) Electrochemical Reduction in a Flow-through Electrochemical System. *Chem. Eng. J.* **2023**, *463*, 142483. [[CrossRef](#)]
7. Yuan, G.; Li, F.; Li, K.; Liu, J.; Li, J.; Zhang, S.; Jia, Q.; Zhang, H. Research Progress on Photocatalytic Reduction of Cr(VI) in Polluted Water. *Bull. Chem. Soc. Jpn.* **2021**, *94*, 1142–1155. [[CrossRef](#)]
8. Meng, Y.; Ma, X.; Luan, F.; Zhao, Z.; Li, Y.; Xiao, X.; Wang, Q.; Zhang, J.; Thandar, S.M. Sustainable Enhancement of Cr(VI) Bioreduction by the Isolated Cr(VI)-Resistant Bacteria. *Sci. Total Environ.* **2022**, *812*, 152433. [[CrossRef](#)]
9. Guo, F.; Peng, C.; Cheng, W.; Sun, X.; Lai, Z.; Yuan, L.; Fan, B.; Gui, Y.; Liu, Y. Photoelectro-Catalytic Oxidation of Monoethanolamine: From the Study of Electrooxidation Mechanism to the Development of High-Efficient Ni-Based Photoelectro-Catalysts. *J. Power Sources* **2024**, *590*, 233793. [[CrossRef](#)]
10. Zhang, R.; Ning, F.; Xu, S.; Zhou, L.; Shao, M.; Wei, M. Oxygen Vacancy Engineering of WO₃ toward Largely Enhanced Photoelectrochemical Water Splitting. *Electrochim. Acta* **2018**, *274*, 217–223. [[CrossRef](#)]
11. Siavash Moakhar, R.; Goh, G.K.L.; Dolati, A.; Ghorbani, M. A Novel Screen-Printed TiO₂ Photoelectrochemical Sensor for Direct Determination and Reduction of Hexavalent Chromium. *Electrochem. Commun.* **2015**, *61*, 110–113. [[CrossRef](#)]
12. Song, H.; Shang, J.; Ye, J.; Li, Q. Investigations on Photoelectrocatalytic Reduction of Cr(VI) over Titanium Dioxide Anode and Metal Cathode. *Thin Solid Film.* **2014**, *551*, 158–162. [[CrossRef](#)]
13. Zhang, Y.; Wang, Q.; Lu, J.; Wang, Q.; Cong, Y. Synergistic Photoelectrochemical Reduction of Cr(VI) and Oxidation of Organic Pollutants by g-C₃N₄/TiO₂-NTs Electrodes. *Chemosphere* **2016**, *162*, 55–63. [[CrossRef](#)]
14. Wang, Q.; Jin, R.; Yin, C.; Wang, M.; Wang, J.; Gao, S. Photoelectrocatalytic Removal of Dye and Cr(VI) Pollutants with Ag₂S and Bi₂S₃ Co-Sensitized TiO₂ Nanotube Arrays under Solar Irradiation. *Sep. Purif. Technol.* **2017**, *172*, 303–309. [[CrossRef](#)]
15. Wang, K.; He, H.; Li, D.; Li, Y.; Li, J.; Li, W. Photoelectrochemical Reduction of Cr (VI) on Plate-like WO₃/BiVO₄ Composite Electrodes under Visible-Light Irradiation: Characteristics and Kinetic Study. *J. Photochem. Photobiol. A Chem.* **2018**, *367*, 438–445. [[CrossRef](#)]
16. Gottesman, R.; Levine, I.; Schleuning, M.; Irani, R.; Abou-Ras, D.; Dittrich, T.; Friedrich, D.; Van De Krol, R. Overcoming Phase-Purity Challenges in Complex Metal Oxide Photoelectrodes: A Case Study of CuBi₂O₄. *Adv. Energy Mater.* **2021**, *11*, 2003474. [[CrossRef](#)]
17. Masoumi, Z.; Tayebi, M.; Lari, S.A.M.; Seo, B.; Lim, C.-S.; Kim, H.-G.; Kyung, D.; Tayebi, M. Photoelectrochemical Performance of a CuBi₂O₄ Photocathode with H₂O₂ as a Scavenger. *Inorganics* **2023**, *11*, 147. [[CrossRef](#)]
18. Xu, Y.; Jian, J.; Li, F.; Liu, W.; Jia, L.; Wang, H. Porous CuBi₂O₄ Photocathodes with Rationally Engineered Morphology and Composition towards High-Efficiency Photoelectrochemical Performance. *J. Mater. Chem. A* **2019**, *7*, 21997–22004. [[CrossRef](#)]
19. Gottesman, R.; Song, A.; Levine, I.; Krause, M.; Islam, A.T.M.N.; Abou-Ras, D.; Dittrich, T.; Van De Krol, R.; Chemseddine, A. Pure CuBi₂O₄ Photoelectrodes with Increased Stability by Rapid Thermal Processing of Bi₂O₃/CuO Grown by Pulsed Laser Deposition. *Adv. Funct. Mater.* **2020**, *30*, 1910832. [[CrossRef](#)]
20. Mao, J.-X.; Wang, J.-C.; Gao, H.; Shi, W.; Jiang, H.-P.; Hou, Y.; Li, R.; Zhang, W.; Liu, L. S-Scheme Heterojunction of CuBi₂O₄ Supported Na Doped P25 for Enhanced Photocatalytic H₂ Evolution. *Int. J. Hydrogen Energy* **2022**, *47*, 8214–8223. [[CrossRef](#)]
21. Meena, B.; Kumar, M.; Hocking, R.K.; Juodkazis, S.; Biju, V.; Subramanyam, P.; Subrahmanyam, C. Exploring CuBi₂O₄ as a Promising Photocathode Material for PEC Water Splitting. *Energy Fuels* **2023**, *37*, 14280–14289. [[CrossRef](#)]
22. Jin, J.; Hu, J.; Qu, J.; Cao, G.; Lei, Y.; Zheng, Z.; Yang, X.; Li, C.M. Reaction Kinetics of Photoelectrochemical CO₂ Reduction on a CuBi₂O₄-Based Photocathode. *ACS Appl. Mater. Interfaces* **2022**, *14*, 17509–17519. [[CrossRef](#)] [[PubMed](#)]

23. Yang, Y.; He, A.; Yang, M.; Zou, Q.; Li, H.; Liu, Z.; Tao, C.; Du, J. Selective Electroreduction of CO₂ to Ethanol over a Highly Stable Catalyst Derived from Polyaniline/CuBi₂O₄. *Catal. Sci. Technol.* **2021**, *11*, 5908–5916. [[CrossRef](#)]
24. Dumitru, R.; Negrea, S.; Păcurariu, C.; Surdu, A.; Ianculescu, A.; Pop, A.; Manea, F. CuBi₂O₄ Synthesis, Characterization, and Application in Sensitive Amperometric/Voltammetric Detection of Amoxicillin in Aqueous Solutions. *Nanomaterials* **2021**, *11*, 740. [[CrossRef](#)] [[PubMed](#)]
25. Arai, T.; Yanagida, M.; Konishi, Y.; Iwasaki, Y.; Sugihara, H.; Sayama, K. Efficient Complete Oxidation of Acetaldehyde into CO₂ over CuBi₂O₄/WO₃ Composite Photocatalyst under Visible and UV Light Irradiation. *J. Phys. Chem. C* **2007**, *111*, 7574–7577. [[CrossRef](#)]
26. Kumar, A.; Rana, A.; Sharma, G.; Dhiman, P. Incorporating Bi Nanodots into CuBi₂O₄/CuFe₂O₄ Heterojunction for a Wide Spectral Synchronous Photoreduction of Hexavalent Chromium and Degradation of Imidacloprid. *Opt. Mater.* **2023**, *140*, 113876. [[CrossRef](#)]
27. Zhang, J.; Ma, Y.; Zhang, W.; Huang, X.; Wang, X.; Huang, Y.; Zhang, P. CuBi₂O₄/Calcined ZnAlBi-LDHs Heterojunction: Simultaneous Removal of Cr(VI) and Tetracycline through Effective Adsorption and Photocatalytic Redox. *J. Clean. Prod.* **2022**, *365*, 132810. [[CrossRef](#)]
28. Dong, P.; Xi, X.; Zhang, X.; Hou, G.; Guan, R. Template-Free Synthesis of Monoclinic BiVO₄ with Porous Structure and Its High Photocatalytic Activity. *Materials* **2016**, *9*, 685. [[CrossRef](#)] [[PubMed](#)]
29. Wen, X.; Luo, W.; Zou, Z. Photocurrent Improvement in Nanocrystalline Cu₂ZnSnS₄ Photocathodes by Introducing Porous Structures. *J. Mater. Chem. A* **2013**, *1*, 15479. [[CrossRef](#)]
30. Zhang, X.; Chen, S.; Guo, F.; Jing, Q.; Huo, P.; Feng, L.; Sun, F.; Chandrasekar, S.; Hao, L.; Liu, B. A Novel Method for Synthesizing Specific Surface Area Modulable G-C₃N₄ Photocatalyst with Maize-like Structure. *Appl. Surf. Sci.* **2024**, *651*, 159224. [[CrossRef](#)]
31. Luo, J.; Wang, Y.; Wang, F.; Li, F.; Li, L.; Zhao, N.; Xiao, F. Aerobic Oxidation of Fluorene to Fluorenone over Copper-Doped Co₃O₄ with a High Specific Surface Area. *ACS Sustain. Chem. Eng.* **2020**, *8*, 2568–2576. [[CrossRef](#)]
32. Yu, Y.; Wu, Z.; Li, J.; Zhu, X.; Ye, D.; Yang, Y.; Wang, H.; An, L.; Chen, R.; Liao, Q. Enhanced Photoelectrochemical Performance of Mesoporous TiO₂ Photoanode Prepared by Multi-Step Evaporation-Induced Self-Assembly Method. *Sep. Purif. Technol.* **2024**, *328*, 125113. [[CrossRef](#)]
33. Li, T.; Dai, L.; Huang, Y.; Pan, S.; Pang, Z.; Zou, J. Spectrophotometric Determination of Cr(VI) in Water Using N, N-Diethyl-p-Phenylenediamine (DPD) as the Indicator. *J. Environ. Chem. Eng.* **2021**, *9*, 105517. [[CrossRef](#)]
34. Song, J.; Wang, H.; Hu, G.; Zhao, S.; Hu, H.; Jin, B. ZnWO₄-Cu System with Enhanced Photocatalytic Activity by Photo-Fenton-like Synergistic Reaction. *Mater. Res. Bull.* **2012**, *47*, 3296–3300. [[CrossRef](#)]
35. Zhang, L.; Nie, Y.; Hu, C.; Qu, J. Enhanced Fenton Degradation of Rhodamine B over Nanoscaled Cu-Doped LaTiO₃ Perovskite. *Appl. Catal. B Environ.* **2012**, *125*, 418–424. [[CrossRef](#)]
36. Nakabayashi, Y.; Nishikawa, M.; Nosaka, Y. Fabrication of CuBi₂O₄ Photocathode through Novel Anodic Electrodeposition for Solar Hydrogen Production. *Electrochim. Acta* **2014**, *125*, 191–198. [[CrossRef](#)]
37. Oropeza, F.E.; Feleki, B.T.; Zhang, K.H.L.; Hensen, E.J.M.; Hofmann, J.P. Influence of Reduced Cu Surface States on the Photoelectrochemical Properties of CuBi₂O₄. *ACS Appl. Energy Mater.* **2019**, *2*, 6866–6874. [[CrossRef](#)]
38. Li, W.; Da, P.; Zhang, Y.; Wang, Y.; Lin, X.; Gong, X.; Zheng, G. WO₃ Nanoflakes for Enhanced Photoelectrochemical Conversion. *ACS Nano* **2014**, *8*, 11770–11777. [[CrossRef](#)] [[PubMed](#)]

Disclaimer/Publisher's Note: The statements, opinions and data contained in all publications are solely those of the individual author(s) and contributor(s) and not of MDPI and/or the editor(s). MDPI and/or the editor(s) disclaim responsibility for any injury to people or property resulting from any ideas, methods, instructions or products referred to in the content.